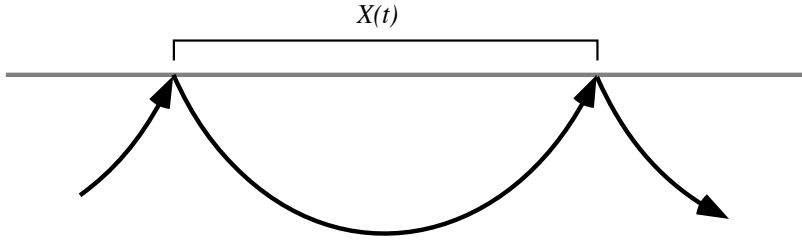


Surface waves and normal modes

Our treatment to this point has been limited to body waves, solutions to the seismic wave equation that exist in whole spaces. However, when free surfaces exist in a medium, other solutions are possible and are given the name *surface waves*. There are two types of surface waves that propagate along Earth's surface: *Rayleigh waves* and *Love waves*. For laterally homogeneous models, Rayleigh waves are radially polarized (P/SV) and exist at any free surface, whereas Love waves are transversely polarized and require some velocity increase with depth (or a spherical geometry). Surface waves are generally the strongest arrivals recorded at teleseismic distances and they provide some of the best constraints on Earth's shallow structure and low-frequency source properties. They differ from body waves in many respects – they travel more slowly, their amplitude decay with range is generally much less, and their velocities are strongly frequency dependent. Surface waves from large earthquakes are observable for many hours, during which time they circle the Earth multiple times. Constructive interference among these orbiting surface waves, together with analogous reverberations of body waves, form the *normal modes*, or *free oscillations* of the Earth. Surface waves and normal modes are generally observed at periods longer than about 10 s, in contrast to the much shorter periods seen in many body wave observations.

8.1 Love waves

Love waves are formed through the constructive interference of high-order SH surface multiples (i.e., SSS , $SSSS$, $SSSSS$, etc.). Thus, it is possible to model Love waves as a sum of body waves. To see this, consider monochromatic plane-wave propagation for the case of a vertical velocity gradient in a laterally homogeneous model, a situation we previously examined in Section 6.4. In this case, a plane wave defined by ray parameter p will turn at the depth where $\beta = 1/p$. Along the



surface the plane wave will propagate with horizontal slowness defined by p . If the surface bouncepoints are separated by a distance $X(t)$, then the travel time along the surface between bouncepoints is given by $pX(p)$. This follows from our definition of a plane wave and does not depend upon the velocity model. In contrast, the travel time along the ray paths is given by $T(p)$ and is a function of the velocity–depth profile. Because these travel times are not the same, destructive interference will occur except at certain fixed frequencies. Along the surface, the phase (0 to 2π) of a harmonic wave will be delayed by $\omega pX(p)$, where ω is the angular frequency of the plane wave. The phase along the ray path is delayed by $\omega T(p) - \pi/2$, where the $-\pi/2$ comes from the WKBJ approximation for the phase advance at the plane-wave turning point (see Section 6.4). The requirement for constructive interference is thus

$$\omega pX(p) = \omega T(p) - \frac{\pi}{2} - n2\pi, \quad (8.1)$$

where n is an integer. Rearranging, we obtain

$$\omega = \frac{n2\pi + \pi/2}{T(p) - pX(p)} = \frac{n2\pi + \pi/2}{\tau(p)}, \quad (8.2)$$

where the delay time $\tau(p) = T(p) - pX(p)$ (see Section 4.3.2). The wave travels along the surface at velocity $c = 1/p$; thus (8.2) defines the $c(\omega)$ function for the Love waves, often termed the *dispersion curve*. The values of ω given for $n = 0$ are termed the fundamental modes; higher modes are defined by larger values of n . The frequency dispersion in the Love waves results from the ray geometry and does not require any frequency dependence in the body wave velocity β . Love wave dispersion is much stronger than the small amount of dispersion in S -wave velocities that results from intrinsic attenuation (see equation (6.91)).

The velocity defined by $c = 1/p$ is the velocity with which the peaks and troughs at a given frequency move along the surface and is termed the *phase velocity*. When the phase velocity varies as a function of frequency, as in (8.2), the wave is dispersed and the group velocity (the velocity that energy propagates) will be different from the phase velocity. In this example, the energy must move along the actual ray paths

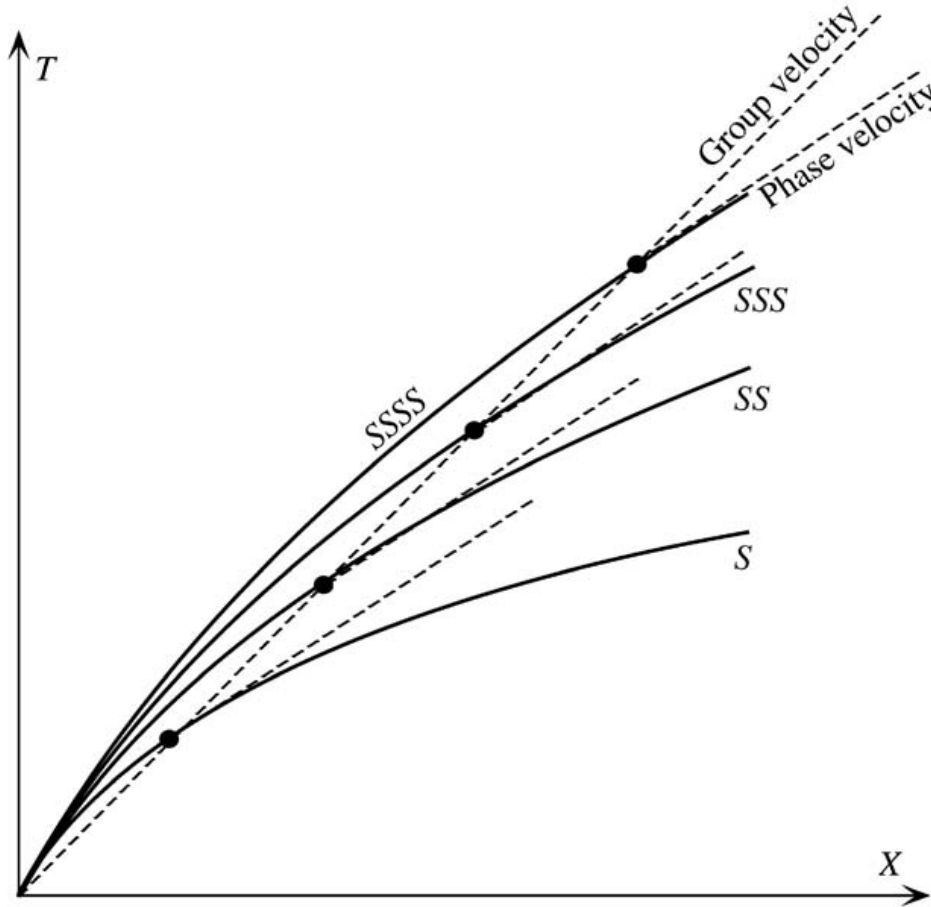


Figure 8.1 Love waves can be constructed as a sum of S surface multiples. The dashed lines show the group and phase velocities at a fixed value of the ray parameter p ; the phase velocity is faster than the group velocity.

and thus the group velocity U is defined by

$$U = \frac{X(p)}{T(p)}. \quad (8.3)$$

For a prograde travel time curve (concave down), U will always be less than c . The relationship between phase and group velocity for Love waves is shown graphically in Figure 8.1 as a sum of SH surface multiples.

The group velocity is also often defined directly from the $c(\omega)$ dispersion relationship. To obtain this form, rewrite (8.1) in terms of the wavenumber $k = \omega p$, producing

$$\omega T - kX = \pi/2 + n2\pi. \quad (8.4)$$

Taking the derivative of this expression, we obtain

$$d\omega T + \omega dT - dk X - k dX = 0$$

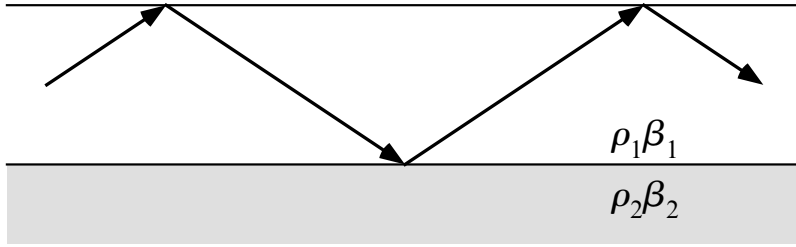


Figure 8.2 Love waves within a homogeneous layer can result from constructive interference between postcritically reflected body waves.

or

$$d\omega T - dk X + \omega dX(dT/dX - k/\omega) = 0. \quad (8.5)$$

Since $p = k/\omega = dT/dX$, the rightmost term drops out, and we have

$$\frac{d\omega}{dk} = \frac{X}{T} = U, \quad (8.6)$$

and we see that the group velocity is also given by $d\omega/dk$.

Equation (8.2) is not very accurate at small values of n since a high frequency approximation was used to determine the phase shift at the turning point. However, it does give some understanding of how Love waves are formed through the positive interference of S surface multiples. More accurate Love wave calculations are generally performed using homogeneous layer techniques. In these methods, the plane wave response of a stack of layers is computed at a series of values of ray parameter; the frequencies of the different Love wave branches are then identified as the eigenvalues of the resulting set of equations.

8.1.1 Solution for a single layer

An exact equation may be derived for Love wave dispersion within a homogeneous layer. Consider a surface layer overlying a higher velocity half-space (Fig. 8.2). Equation (8.2) is still applicable, provided we replace the approximate $\pi/2$ phase shift at the turning point with the phase shift, $\phi_{\hat{S}\hat{S}}$, resulting from the SH reflection off the bottom of the layer:

$$\omega = \frac{n2\pi - \phi_{\hat{S}\hat{S}}}{\tau(p)}. \quad (8.7)$$

From (4.33), we may express the delay time τ as

$$\tau(p) = 2h\sqrt{1/\beta_1^2 - p^2}, \quad (8.8)$$

where h is the layer thickness and β_1 is the shear velocity in the top layer. For postcritical reflections, it can be shown from (6.46) and (6.59) that

$$\phi_{\tilde{S}\tilde{S}} = -2 \tan^{-1} \left[\frac{\mu_2 \sqrt{p^2 - 1/\beta_2^2}}{\mu_1 \sqrt{1/\beta_1^2 - p^2}} \right]. \quad (8.9)$$

Substituting (8.8) and (8.9) into (8.7), we have

$$2h\omega \sqrt{1/\beta_1^2 - p^2} - n2\pi = 2 \tan^{-1} \left[\frac{\mu_2 \sqrt{p^2 - 1/\beta_2^2}}{\mu_1 \sqrt{1/\beta_1^2 - p^2}} \right]$$

or

$$\tan \left[h\omega \sqrt{1/\beta_1^2 - p^2} \right] = \frac{\mu_2 \sqrt{p^2 - 1/\beta_2^2}}{\mu_1 \sqrt{1/\beta_1^2 - p^2}}. \quad (8.10)$$

This defines the dispersion curves for Love wave propagation within the layer. Note that the phase velocity, $c = 1/p$, varies between β_1 and β_2 ($c > \beta_2$ is not postcritical). For every value of c , there are multiple values of ω because of the periodicity in the tangent function. The smallest of the ω values defines the fundamental mode, the second smallest is the first higher mode, etc. There is no analytical solution to (8.10) for c ; the $c(\omega)$ values must be determined numerically (see Exercise 8.1).

8.2 Rayleigh waves

For SH polarized waves, the reflection coefficient at the free surface is one, and the interference between the downgoing SH waves and those turned back toward the surface produces Love waves. The P/SV system is more complicated because the surface reflections involve both P and SV waves. In this case, the upgoing and downgoing body waves do not sum constructively to produce surface waves. However, a solution is possible for inhomogeneous waves trapped at the interface; the resulting surface waves are termed *Rayleigh waves*. The displacements of Love and Rayleigh waves are compared in Figure 8.3.

Let us begin by examining what occurs when P and SV waves interact with a free surface. For a laterally homogeneous medium, the displacements for harmonic

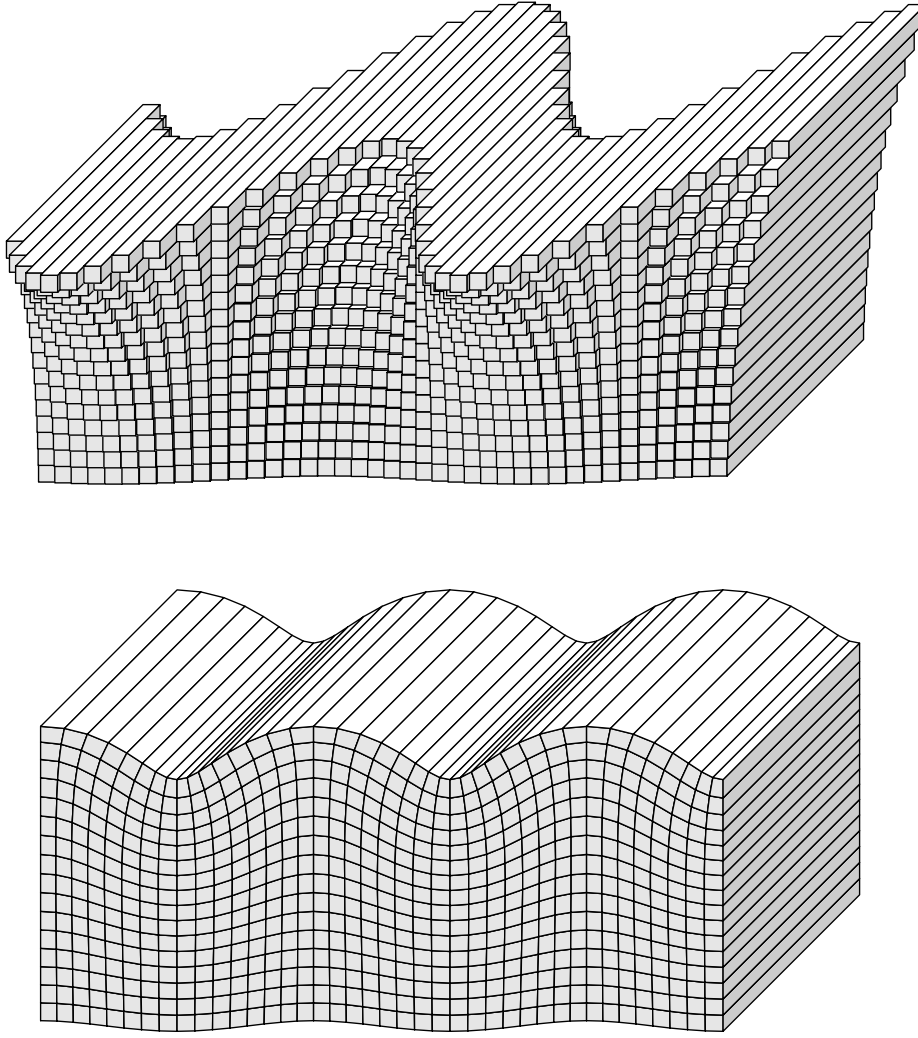


Figure 8.3 Fundamental Love (top) and Rayleigh (bottom) surface wave displacements (highly exaggerated) for horizontal propagation across the page. Love waves are purely transverse motion, whereas Rayleigh waves contain both vertical and radial motion. In both cases, the wave amplitude decays strongly with depth.

plane waves propagating in the $+x$ direction are given by

$$\mathbf{u} = \mathbf{A}e^{-i\omega(t-px-\eta z)}, \quad (8.11)$$

where p is the horizontal slowness and $\eta = \sqrt{1/c^2 - p^2}$ is the vertical slowness for wave velocity c . From Section 3.3.1, recall that we may express the displacement in terms of a P -wave scalar potential ϕ and a S -wave vector potential Ψ , that is,

$$\mathbf{u} = \nabla\phi + \nabla \times \Psi. \quad (8.12)$$

Now from (8.11), consider plane wave solutions for ϕ and Ψ_y (the only part of Ψ that produces SV motion for plane wave propagation in the x direction):

$$\phi = Ae^{-i\omega(t-px-\eta_\alpha z)}, \quad (8.13)$$

$$\Psi_y = Be^{-i\omega(t-px-\eta_\beta z)}, \quad (8.14)$$

where A and B are the amplitudes of the P and SV waves respectively, and the vertical slownesses are given by

$$\eta_\alpha = (1/\alpha^2 - p^2)^{1/2}, \quad (8.15)$$

$$\eta_\beta = (1/\beta^2 - p^2)^{1/2}. \quad (8.16)$$

The ray parameter p is constant; both P and SV are assumed to have the same horizontal slowness. Noting that ∂_y and u_y are zero for our P/SV plane wave geometry, the P -wave displacements are

$$u_x^P = \partial_x \phi = pAi\omega e^{-i\omega(t-px-\eta_\alpha z)}, \quad (8.17)$$

$$u_z^P = \partial_z \phi = \eta_\alpha Ai\omega e^{-i\omega(t-px-\eta_\alpha z)}, \quad (8.18)$$

and the SV -wave displacements are

$$u_x^S = -\partial_z \Psi_y = -\eta_\beta Bi\omega e^{-i\omega(t-px-\eta_\beta z)}, \quad (8.19)$$

$$u_z^S = \partial_x \Psi_y = pBi\omega e^{-i\omega(t-px-\eta_\beta z)}. \quad (8.20)$$

Now consider the boundary conditions at a free surface $z = 0$. Both the normal and shear tractions must vanish: $\tau_{xz} = \tau_{zz} = 0$. From (3.13), we have

$$\tau_{xz} = \mu(\partial_z u_x + \partial_x u_z), \quad (8.21)$$

$$\tau_{zz} = \lambda(\partial_x u_x + \partial_z u_z) + 2\mu\partial_z u_z. \quad (8.22)$$

Substituting (8.17)–(8.20) into (8.21) and (8.22), we obtain

$$\tau_{xz}^P = -A(2\mu p\eta_\alpha)\omega^2 e^{-i\omega(t-px-\eta_\alpha z)}, \quad (8.23)$$

$$\tau_{zz}^P = -A[(\lambda + 2\mu)\eta_\alpha^2 + \lambda p^2]\omega^2 e^{-i\omega(t-px-\eta_\alpha z)}, \quad (8.24)$$

$$\tau_{xz}^S = -B\mu(p^2 - \eta_\beta^2)\omega^2 e^{-i\omega(t-px-\eta_\beta z)}, \quad (8.25)$$

$$\tau_{zz}^S = -B(2\mu\eta_\beta p)\omega^2 e^{-i\omega(t-px-\eta_\beta z)}. \quad (8.26)$$

At the free surface, we require

$$\tau_{xz} = \tau_{xz}^P + \tau_{xz}^S = 0, \quad (8.27)$$

$$\tau_{zz} = \tau_{zz}^P + \tau_{zz}^S = 0. \quad (8.28)$$

Substituting (8.23)–(8.26) into (8.27) and (8.28) at $z = 0$, and canceling the common terms, we obtain

$$A(2p\eta_\alpha) + B(p^2 - \eta_\beta^2) = 0, \quad (8.29)$$

$$A[(\lambda + 2\mu)\eta_\alpha^2 + \lambda p^2] + B(2\mu\eta_\beta p) = 0. \quad (8.30)$$

The equations for τ_{zz} can be written in terms of the P and S velocities by substituting $\lambda + 2\mu = \rho\alpha^2$, $\mu = \rho\beta^2$, and $\lambda = \rho(\alpha^2 - 2\beta^2)$ to give

$$A[2p\eta_\alpha] + B[p^2 - \eta_\beta^2] = 0, \quad (8.31)$$

$$A[\alpha^2(\eta_\alpha^2 + p^2) - 2\beta^2 p^2] + B[2\beta^2 \eta_\beta p] = 0. \quad (8.32)$$

This coupled set of equations describes the free surface boundary condition for P - and SV -waves with horizontal slowness p . Recall that the vertical slownesses are given by $\eta_\alpha = (1/\alpha^2 - p^2)^{1/2}$ and $\eta_\beta = (1/\beta^2 - p^2)^{1/2}$. When $p < 1/\alpha$, there are two real solutions, a positive value of η_α for downgoing P waves and a negative value for upgoing P waves (assuming the z axis points downward). Similarly, when $p < 1/\beta$, then η_β is real and there exist both downgoing and upgoing SV waves. By defining different amplitude coefficients for the downgoing and upgoing waves, one could use (8.31) and (8.32) to solve for the P/SV reflection coefficients at the free surface.

However, our interest is in the case where $p > \beta^{-1} > \alpha^{-1}$ and both η_α and η_β are imaginary. From (8.11), if we factor out the depth dependence, we obtain

$$\mathbf{u} = \mathbf{A} e^{i\omega\eta z} e^{-i\omega(t - px)}, \quad (8.33)$$

and we see that imaginary values of η will lead to real values in the exponent. In this case we have the evanescent waves discussed in Chapter 6, for which amplitude grows or decays exponentially as a function of depth. The sign of η is chosen to give the solution that decays away from $z = 0$. For single imaginary values of η_α and η_β , the linear system of equations for A and B given in (8.31) and (8.32) has a non-trivial solution only when the determinant vanishes, that is, when

$$(p^2 - \eta_\beta^2) [\alpha^2(\eta_\alpha^2 + p^2) - 2\beta^2 p^2] - 4\beta^2 p^2 \eta_\alpha \eta_\beta = 0. \quad (8.34)$$

Substituting for η_α and η_β , we can express this entirely in terms of p and the P and S velocities:

$$\left(2p^2 - \frac{1}{\beta^2}\right)^2 + 4p^2 \left(\frac{1}{\alpha^2} - p^2\right)^{1/2} \left(\frac{1}{\beta^2} - p^2\right)^{1/2} = 0, \quad (8.35)$$

after canceling a common factor of β^2 . For imaginary η_α and η_β ($p > \beta^{-1} > \alpha^{-1}$), this can be rewritten as

$$\left(2p^2 - \frac{1}{\beta^2}\right)^2 - 4p^2 \left(p^2 - \frac{1}{\alpha^2}\right)^{1/2} \left(p^2 - \frac{1}{\beta^2}\right)^{1/2} = 0. \quad (8.36)$$

This is termed the *Rayleigh function* and has a single solution, with the exact value of p depending upon β and α . The corresponding phase velocity, $c = 1/p$, is always slightly less than the shear velocity, with $c = 0.92\beta$ for a Poisson solid. This result, obtained by Rayleigh over 100 years ago, shows that it is possible for two coupled inhomogeneous P and SV waves to propagate along the surface of a half-space.

By substituting the solution for p into (8.15), (8.16), (8.31), and (8.32), we may obtain the relative amplitudes of the P and SV components, and then substitution into (8.17)–(8.20) will give the vertical and horizontal displacements. Rayleigh wave particle motion for the fundamental mode is shown in Figure 8.4. The vertical

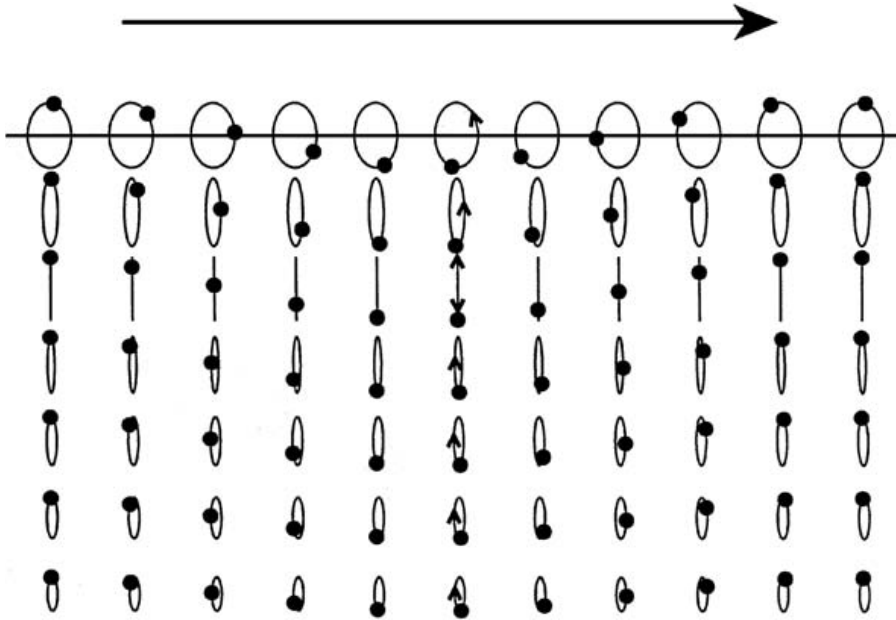


Figure 8.4 Particle motion for the fundamental Rayleigh mode in a uniform half-space, propagating from left to right. One horizontal wavelength (Λ) is shown; the dots are plotted at a fixed time point. Motion is counter clockwise (retrograde) at the surface, changing to purely vertical motion at a depth of about $\Lambda/5$, and becoming clockwise (prograde) at greater depths. Note that the time behavior at a fixed distance is given by looking from right to left in this plot.

and horizontal components are out of phase by $\pi/2$; the resulting elliptical motion changes from *retrograde* at the surface to *prograde* at depth, passing through a node at which there is no horizontal motion. For Rayleigh waves propagating along the surface of a uniform half-space there is no velocity dispersion (since there is no scale length in the model). However, in the Earth velocity dispersion results from the vertical velocity gradients in the crust and upper mantle; longer period waves travel faster since they sense the faster material at greater depths. As in the case of Love waves, Rayleigh wave dispersion curves for vertically stratified media may be computed using propagator matrix methods.

8.3 Dispersion

When different frequency components travel at different phase velocities, pulse shapes will not stay the same as they travel but will become dispersed as the frequencies separate. This leads to interference effects that cancel the wave energy except at particular times defined by the group velocity of the wave. This may be illustrated by considering the sum of two harmonic waves of slightly different frequency and wavenumber:

$$u(x, t) = \cos(\omega_1 t - k_1 x) + \cos(\omega_2 t - k_2 x). \quad (8.37)$$

Relative to an average frequency ω and wavenumber k , we have

$$\omega_1 = \omega - \delta\omega, \quad k_1 = k - \delta k, \quad (8.38)$$

$$\omega_2 = \omega + \delta\omega, \quad k_2 = k + \delta k. \quad (8.39)$$

Substituting into (8.37), we obtain

$$\begin{aligned} u(x, t) &= \cos(\omega t - \delta\omega t - kx + \delta kx) + \cos(\omega t + \delta\omega t - kx - \delta kx) \\ &= \cos[(\omega t - kx) - (\delta\omega t - \delta kx)] + \cos[(\omega t - kx) + (\delta\omega t - \delta kx)] \\ &= 2 \cos(\omega t - kx) \cos(\delta\omega t - \delta kx), \end{aligned} \quad (8.40)$$

where we have used the identity $2 \cos A \cos B = \cos(A + B) + \cos(A - B)$. The resulting waveform consists of a signal with the average frequency ω whose amplitude is *modulated* by a longer period wave of frequency $\delta\omega$ (Fig. 8.5).

In acoustics, this phenomenon is termed *beating* and may be observed when two musical notes are slightly out of tune. The short-period wave travels at velocity ω/k and the longer period envelope travels at velocity $\delta\omega/\delta k$. The former is the phase velocity c ; the latter is the group velocity U . In the limit as $\delta\omega$ and δk approach

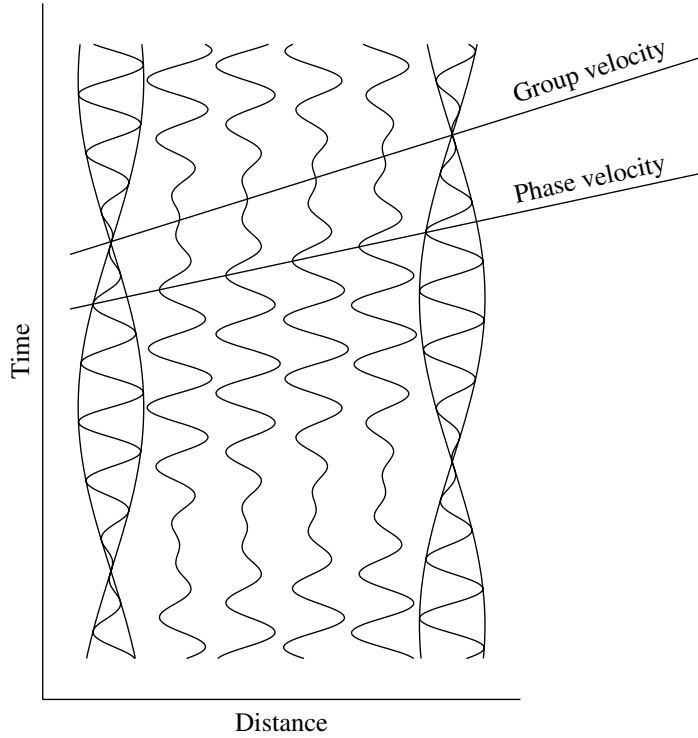


Figure 8.5 The sum of two waves of slightly different frequencies results in a modulated wave. The group velocity is the velocity of the wave packets; the phase velocity is the velocity of the individual peaks.

zero, we thus have

$$U = \frac{d\omega}{dk}, \quad (8.41)$$

which agrees with our previous result in (8.6). Using the various relationships between the harmonic wave parameters (see Table 3.1), the group velocity may be alternatively expressed as

$$U = \frac{d\omega}{dk} = c + k \frac{dc}{dk} = c \left(1 - k \frac{dc}{d\omega} \right)^{-1}. \quad (8.42)$$

For Earth, the phase velocity c of both Love and Rayleigh waves generally increases with period; thus $dc/d\omega$ is negative and from (8.42) it follows that the group velocity is less than the phase velocity ($U < c$). Figure 8.6 plots Love and Rayleigh dispersion curves computed from the PREM model. A minimum or maximum point on the group velocity dispersion curve will result in energy from a range of periods arriving at nearly the same time. This is termed an *Airy phase* and occurs in Earth for Rayleigh waves at periods of about 50 and 240 s.

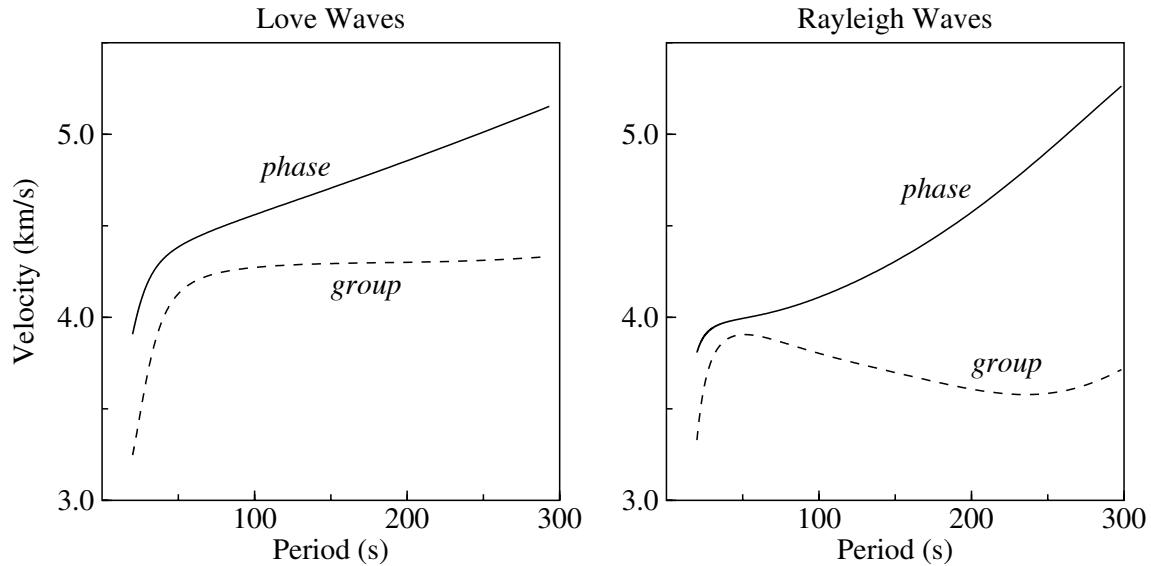


Figure 8.6 Fundamental Love and Rayleigh dispersion curves computed from the isotropic PREM model (courtesy of Gabi Laske).

8.4 Global surface waves

Love and Rayleigh waves in Earth travel along great circle paths radiating away from the source. Since they are confined to the surface of a sphere, geometrical spreading effects are reduced compared to body waves (which spread within a volume). At a given receiver location, the first surface wave arrival will travel along the minor (shorter) great circle arc and a later arrival will result from the major arc path on the opposite side of Earth (Fig. 8.7). The second arrival is due to surface waves that have passed through the *antipode*, the point directly opposite the source. The first and second arriving Love wave arrivals are termed *G1* and *G2*, respectively, while the corresponding Rayleigh waves are called *R1* and *R2*. The waves do not stop at the receiver, but continue traveling around the globe and these multiple orbits produce a series of later arrivals that can be observed for many hours following large earthquakes. The odd-numbered surface waves (e.g., *R1*, *R3*, *R5*, etc.) leave the source in the minor arc direction, while the even numbered waves depart in the major arc direction.

This is illustrated in Figure 8.8, which plots three components of motion from an earthquake at 230 km depth in the Tonga subduction zone recorded by the IRIS/IDA station NNA in Peru. Notice that the *SH* polarized Love wave arrivals appear most prominently on the transverse component, while the *P/SV* polarized Rayleigh waves are seen mostly on the vertical and radial components. Attenuation of surface waves can be seen in the decay of the amplitude of the arrivals with time.

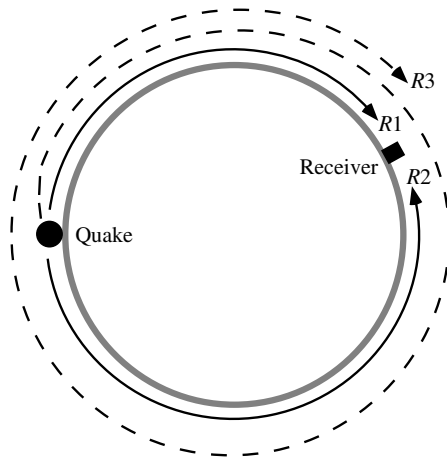


Figure 8.7 Ray paths for the first three Rayleigh wave arrivals.

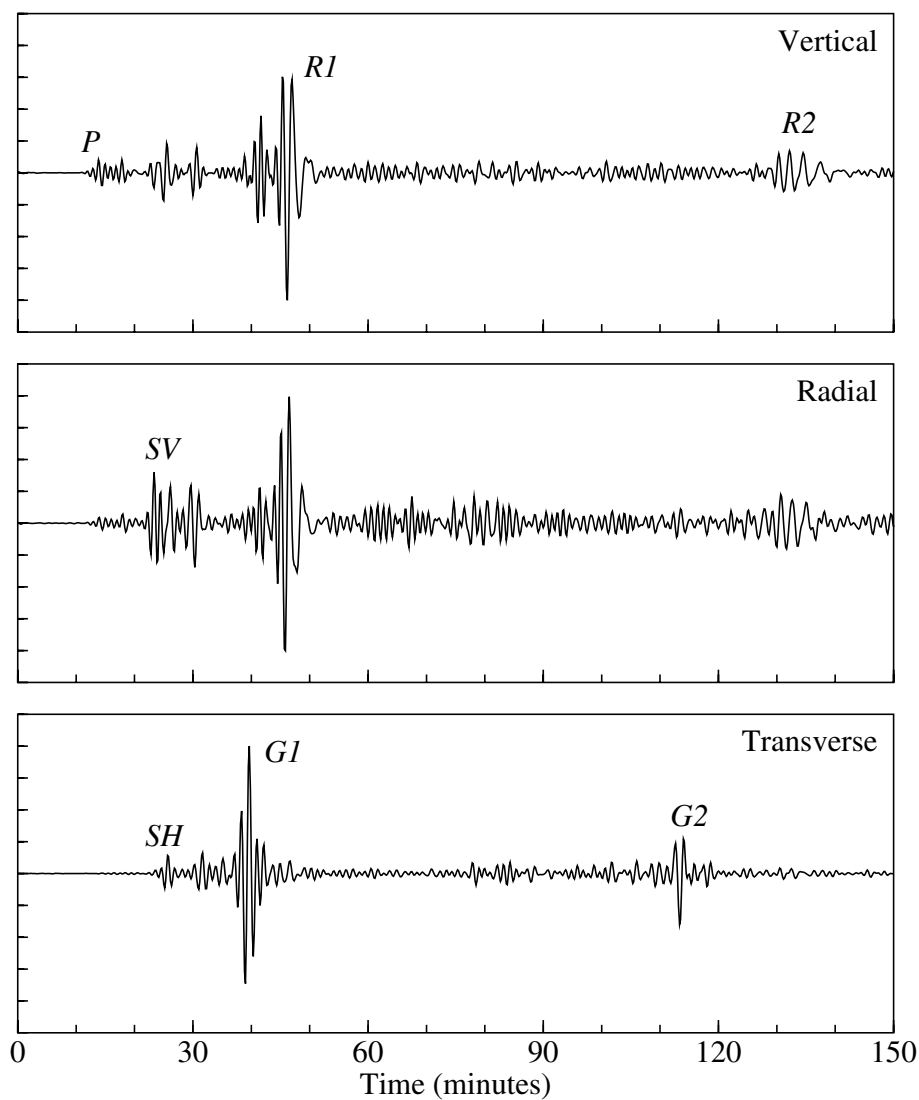


Figure 8.8 The vertical, radial, and transverse components of motion for a March 11, 1989, earthquake at 230 km depth in the Tonga trench recorded at IRIS/IDA station NNA in Peru. *P*, *SV*, and Rayleigh waves are most visible on the vertical and radial components; *SH* and Love waves appear on the transverse component.

At long periods, Rayleigh waves are sufficiently coherent that it is possible to stack records from many different events to produce a global picture (Fig. 8.9) of the seismic wavefield that images the surface wave arrivals (Shearer, 1994). This vertical-component image illustrates many of the concepts that we have developed in this chapter. The dispersion of the Rayleigh waves is clearly apparent, particularly in the later part of the image. Very long period (≥ 300 s) waves travel the fastest, arriving before the pronounced shorter-period banding in the Airy phase. The high amplitude of the Airy phase results from a local minimum in the group velocity dispersion curve near 240 s. The difference between phase and group velocity can be seen clearly in the image of the Airy phase. The lines of constant phase, defined by the peaks and troughs in the seismograms, are not parallel to the overall direction of energy transport. Rather, they cut across at a slightly more horizontal orientation, since the phase velocity is higher than the group velocity.

The major *P* and *SV* body-wave phases can also be seen in this image, in the triangular shaped region before the first Rayleigh wave (*R1*). Additional body-wave arrivals are visible between *R1* and the second Rayleigh wave (*R2*). These include some *P* phases, but most prominent are the high-order *S* surface multiples and the families of *S*-to-*P* converted phases that they spawn upon each surface reflection. These can be traced to beyond 720° and are the major source of seismic energy between the Rayleigh wave arrivals. In the surface wave literature, these arrivals are termed overtone packets and are sometimes referred to as *X* phases (e.g., Tanimoto, 1987).

8.5 Observing surface waves

Surface waves are generally the strongest arrivals at teleseismic distances and contain a great deal of information about crust and upper mantle structure as well as the seismic source. Much of the power of surface wave observations comes from the fact that velocity can be measured at a number of different frequencies from a single seismogram, providing direct constraints on the velocity versus depth profile everywhere along the source–receiver path. In contrast, the corresponding body wave observations provide only a single travel time per phase, and recovering the complete velocity structure requires stations at a wide range of source–receiver distances.

A major goal in most surface wave studies is to determine the group or phase velocity at a number of periods. This can be done in several ways. If the location and origin time of the source are known, then the group velocity may be estimated from a surface wave record at a single station by measuring the travel time to the station for energy at a particular frequency. This can be done by applying narrow

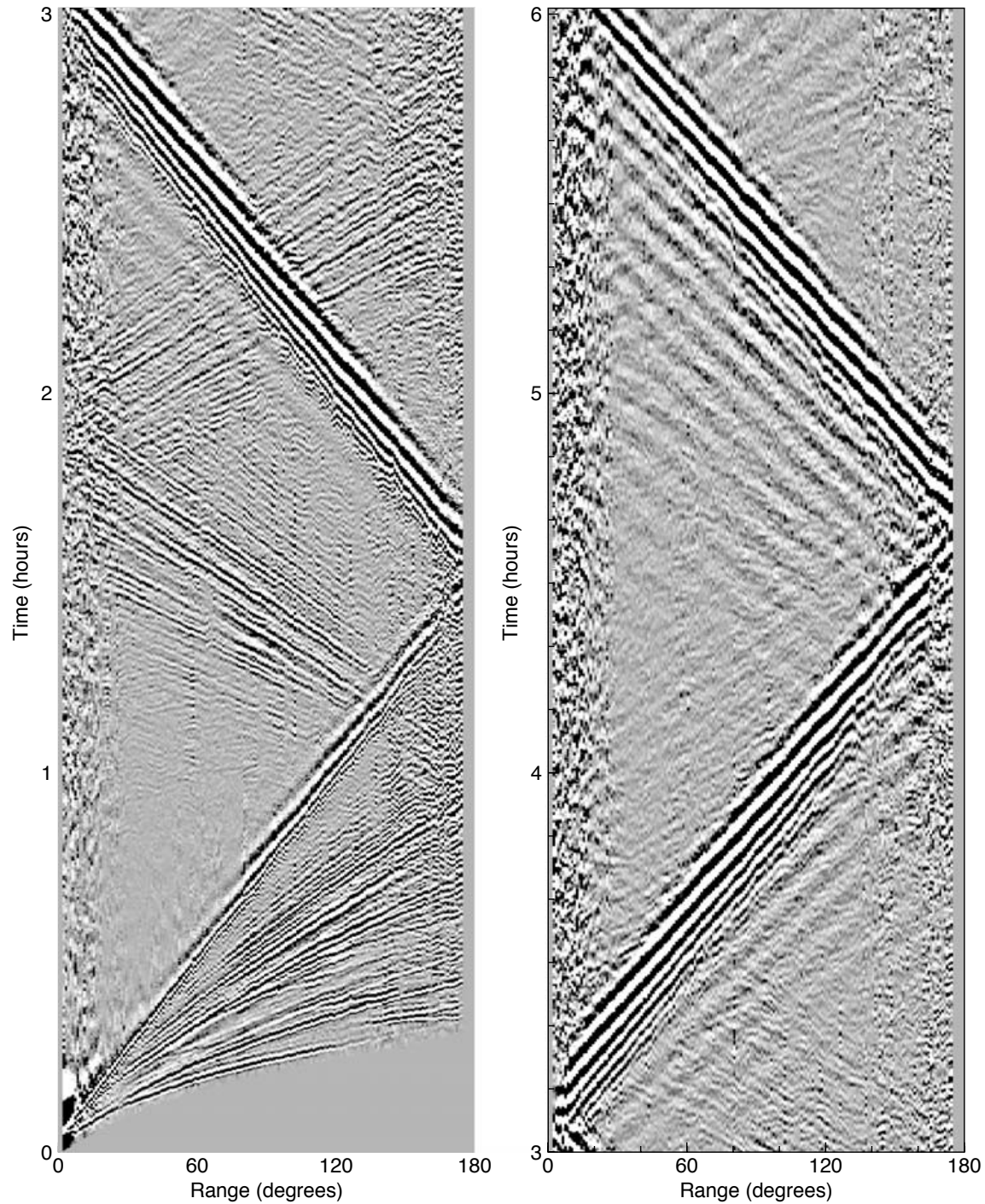


Figure 8.9 An image of Earth's long-period seismic response on vertical component seismographs as a function of time and distance to an earthquake. Positive amplitudes are shown as black, and negative amplitudes are shown as white. The Rayleigh wave arrivals *R1* and *R2* are visible in the left panel showing the first 3 hours of data, whereas *R3* and *R4* are seen on the right panel.

passband filters to the record to isolate the wave packet for a target frequency, or, more crudely, by measuring the time between successive peaks in a single dispersed seismogram. The same approach can be used to determine the group velocity between two stations along a great circle ray path through the source by measuring the difference in the arrival times at the stations. In this case (the *two-station method*), precise details of the source are not required, provided the location is approximately correct.

Many modern surface wave analyses measure the phase velocity rather than the group velocity. This is done by computing the Fourier spectrum of the record to determine the phase of each frequency component. If the phase is known at the source (this requires the focal mechanism or moment tensor for the event), then phase velocity measurements are possible from a single receiver; alternatively the two-station method can be used to determine the phase velocity between a pair of receivers. The tricky part of phase velocity measurements is that the observed phase ϕ at a particular frequency varies only between 0 and 2π and there will typically be many cycles between observation points, so that the total phase shift Φ is actually $2\pi n + \phi$, where n is an integer.

For example, consider measuring the Rayleigh wave phase velocity in Fig. 8.9 at a period of 240 s (close to the dominant period of the high-amplitude Airy phase) using stations at 90° and 120° . Phase measurements at these ranges alone do not tell us how many cycles, n , occurred between the stations; the phase velocity cannot be determined without independent knowledge of n . At long periods this is not a significant problem since n can be accurately estimated from standard one-dimensional Earth models. However, at shorter periods it becomes increasingly difficult to calculate n with confidence, since lateral velocity variations in the upper mantle cause n to vary with position as well as range. In this case, a useful approach is to measure the phase velocity at the longest periods first, and then gradually move to shorter periods, keeping track of the total accumulated phase shift Φ . This will work provided the phase velocity dispersion curve is a smooth and continuous function of frequency.

Comprehensive studies of surface wave phase velocities, using a global distribution of sources and receivers, can be used to invert for maps of phase velocity for both Love and Rayleigh waves. This is done separately for each period using techniques analogous to the body-wave velocity inversion problem discussed in Chapter 5. The structure seen in these maps is related to Earth's lateral velocity variations; the depth dependence in this heterogeneity is constrained by the results at different periods. Inverting surface-wave phase velocity observations is currently one of the best ways to resolve three-dimensional velocity variations in the upper few hundred kilometers of the mantle.

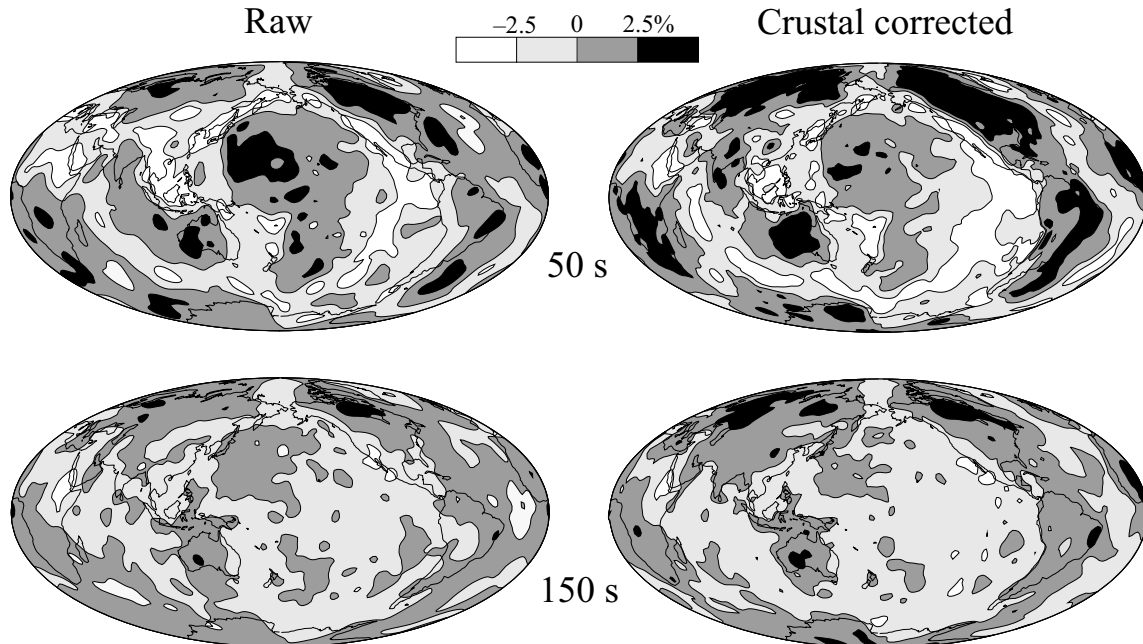


Figure 8.10 Rayleigh wave phase velocity at (top) 50 s and (bottom) 150 s period. The right panels have been corrected for crustal thickness variations using the model CRUST 2.0 (Laske *et al.*, <http://mahi.ucsd.edu/Gabi/rem.dir/crust/crust2.html>). Velocity perturbations are contoured at 2.5% intervals, with black indicating regions that are 2.5% faster than average, and white indicating velocities over 2.5% slower than average. Maps produced by Guy Masters (personal communication) using measurements from Ekström *et al.* (1997).

Figure 8.10 plots maps of Rayleigh wave phase velocity at 50 and 150 s period. Notice the ocean-continent signal is enhanced after corrections are applied for variations in crustal thickness. In general, the thicker crust beneath continents compared to the oceans causes slower surface-wave velocities, but this is counteracted by generally faster upper-mantle velocities beneath continents, which are especially strong in shield regions. When corrections for variations in crustal properties are applied (to obtain what the velocity would be for a globally uniform crust), the fast continental roots become even more prominent, particularly at shorter periods, which are more sensitive to shallow structure. Global mantle tomography models rely heavily on surface-wave analyses to constrain upper-mantle heterogeneity. Notice the similarity between the 50 s crustal-corrected phase velocity map and the velocity structure at 150 km depth in Figure 1.7.

8.6 Normal modes

Thus far we have considered the propagation of body and surface waves largely as if the Earth were of infinite extent. However, the Earth is a finite body in which

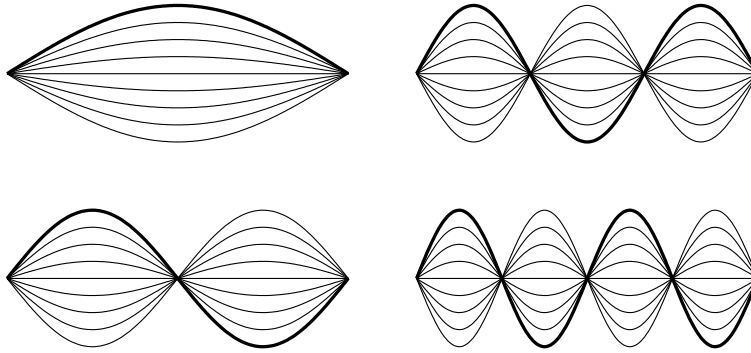


Figure 8.11 The first four modes of vibration of a string between fixed endpoints.

all wave motions must be confined. Body waves are reflected from the surface; surface waves orbit along great circle paths. At a particular point on the Earth's surface, there will be a series of arrivals of different seismic phases. The timing between these arrivals will result in constructive and destructive interference such that only certain frequencies will resonate over long time intervals. These resonant frequencies are termed Earth's *normal modes* and provide a way of representing wave propagation that is an alternative to the traveling wave approach.

The vibrations of a string fixed at both ends provide an analogy that may be familiar from your physics classes. The string will resonate only at certain frequencies (Fig. 8.11). These are termed the *standing waves* for the string and any motion of the string can be expressed as a weighted sum of the standing waves. This is an eigenvalue problem; the resonant frequencies are termed the *eigenfrequencies*; the string displacements are termed the *eigenfunctions*. In a musical instrument the lowest frequency is called the fundamental mode; the higher modes are the overtones or *harmonics*. For the vibrating string, the eigenfunctions are sines and cosines and it is natural to use a Fourier representation.

Normal modes for the Earth are also specified by their eigenfrequencies and eigenfunctions. A detailed treatment of normal mode theory for the Earth is beyond the scope of this book, and computation of eigensolutions for realistic Earth models is a formidable task. However, it is useful to remember some of the properties of the eigenfunctions of any vibrating system:

1. They are complete. Any wave motion within the Earth may be expressed as a sum of normal modes with different excitation factors.
2. They are orthogonal in the sense that the integral over the volume of the Earth of the product of any two eigenfunctions is zero. This implies that the normal mode representation of wave motion is unique.

What do Earth's normal modes look like? For a spherically symmetric solid, it can be shown that there are two distinctly different types of modes: *spheroidal modes*,

which are analogous to P/SV and Rayleigh wave motion, and *toroidal modes*, which are analogous to SH and Love wave motion. The Earth's departures from spherical symmetry mean that this separation is not complete, but it is a very good first-order approximation. Toroidal modes involve no radial motion and are sensitive only to the shear velocity, whereas spheroidal modes have both radial and horizontal motion and are sensitive to both compressional and shear velocities. Spheroidal mode observations at long periods are also sensitive to gravity and provide the best direct seismic constraints on Earth's density structure.

The lateral variations in normal mode eigenfunctions are best described in terms of *spherical harmonics*, which provide an orthogonal set of basis functions on a spherical surface (spherical harmonics are useful in many areas of geophysics for representing functions on the surface of a sphere, and descriptions are available in many of the standard texts; see Aki and Richards (1980, 2002) or Lay and Wallace (1995) for treatments focusing on seismology). A common normalization for the spherical harmonics is

$$Y_l^m(\theta, \phi) = (-1)^m \left[\frac{2l+1}{4\pi} \frac{(l-m)!}{(l+m)!} \right]^{1/2} P_l^m(\cos \theta) e^{im\phi} \quad (8.43)$$

where θ and ϕ are spherical polar coordinates (θ is the polar angle) and P_l^m is the *associated Legendre function*. The spherical harmonic function is written as Y_l^m , where l is termed the *angular order number* and m is the *azimuthal order number*. The index l is sometimes also termed the *spherical harmonic degree* and is zero or a positive integer up to any value. The angular order number, m , may take on $2l+1$ integer values between $\pm l$. The order numbers determine the number of lines of zero crossings that are present in the function. The total number of zero crossings is given by l ; the number of zero crossings through the pole is given by $|m|$. Figure 8.12 plots examples of Y_l^m for some of the lower harmonic degrees.

Note that the harmonics are defined relative to a particular coordinate system and depend upon the location of the poles. If the coordinate system is rotated, any spherical harmonic function in the old coordinate system may be expressed as a sum of spherical harmonics of the same l but differing m in the new coordinate system. A rotation of coordinates does not affect the angular order number but will change the relative weights of the azimuthal order numbers. For example, a rotation of 90° can change Y_1^0 to Y_1^1 .

Expansions of global observations in terms of spherical harmonics are common in geophysics. Examples include Earth's surface geoid and seismic velocity perturbations at a particular depth. For Earth's normal modes, we are interested in displacement, which is a vector quantity and most conveniently expressed in terms

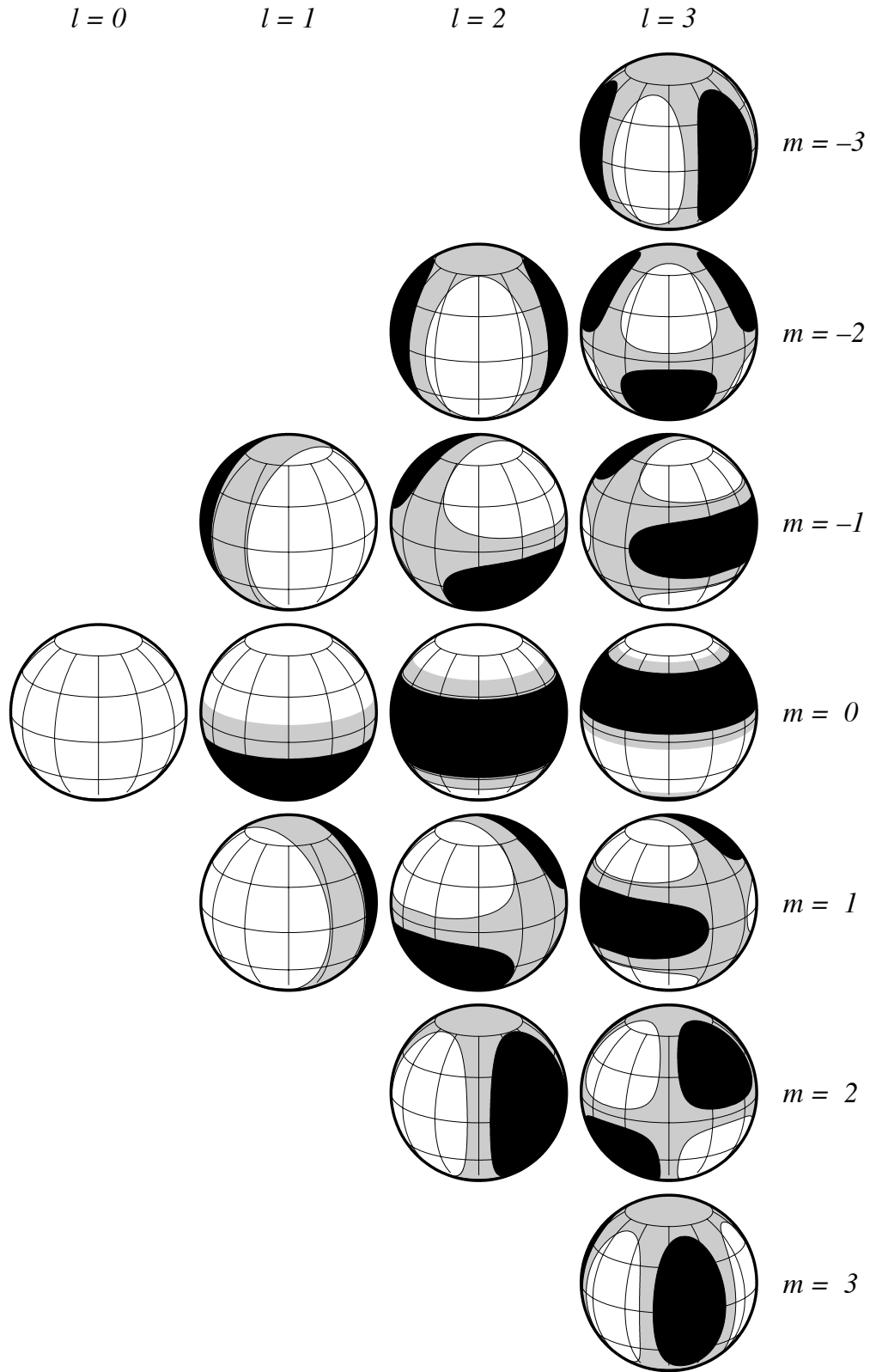


Figure 8.12 Spherical harmonic functions Y_l^m up to degree $l = 3$. Positive values are shown as white, negative as black, with near-zero values as gray. There are $2l + 1$ values of m at each degree. Note that the negative m harmonics are rotated versions of the positive m harmonics.

of the *vector spherical harmonics*, which are defined as

$$\mathbf{R}_l^m(\theta, \phi) = Y_l^m \hat{\mathbf{r}} \quad (8.44)$$

$$\mathbf{S}_l^m(\theta, \phi) = \frac{1}{\sqrt{l(l+1)}} \left[\frac{\partial Y_l^m}{\partial \theta} \hat{\boldsymbol{\theta}} + \frac{1}{\sin \theta} \frac{\partial Y_l^m}{\partial \phi} \hat{\boldsymbol{\phi}} \right] \quad (8.45)$$

$$\mathbf{T}_l^m(\theta, \phi) = \frac{1}{\sqrt{l(l+1)}} \left[\frac{1}{\sin \theta} \frac{\partial Y_l^m}{\partial \phi} \hat{\boldsymbol{\theta}} - \frac{\partial Y_l^m}{\partial \theta} \hat{\boldsymbol{\phi}} \right] \quad (8.46)$$

where $\hat{\mathbf{r}}$, $\hat{\boldsymbol{\theta}}$, and $\hat{\boldsymbol{\phi}}$ are unit vectors in the r , θ , and ϕ directions, respectively. The vector fields associated with Earth's spheroidal motions can be expressed in terms of \mathbf{R} and \mathbf{S} , while the toroidal motions are expressed with \mathbf{T} .

Earth's normal modes are specified in terms of the spherical harmonic order numbers l and m and a *radial order number*, n , that describes the number of zero crossings in radius that are present. Toroidal modes are thus designated ${}_nT_l^m$ and spheroidal modes as ${}_nS_l^m$. The solutions for $n = 0$ are called the fundamental modes; the solutions for $n > 0$ are termed overtones. For a spherically symmetric Earth the eigenfrequencies at constant n and l are identical for all values of m and it is common to denote modes only by their radial and angular order numbers, that is, as ${}_nT_l$ and ${}_nS_l$ and the corresponding frequencies as ${}_n\omega_l$.

The fundamental spheroidal mode ${}_0S_0$ is termed the “breathing” mode and represents a simple expansion and contraction of the Earth. It has a period of about 20 minutes. ${}_0S_1$ is not used in seismology since it describes a shift in the center of mass of the Earth; this cannot result from purely internal forces. ${}_0S_2$ has a period of about 54 minutes and represents an oscillation between an ellipsoid of horizontal and vertical orientation (Fig. 8.13). This is sometimes termed the “rugby” mode

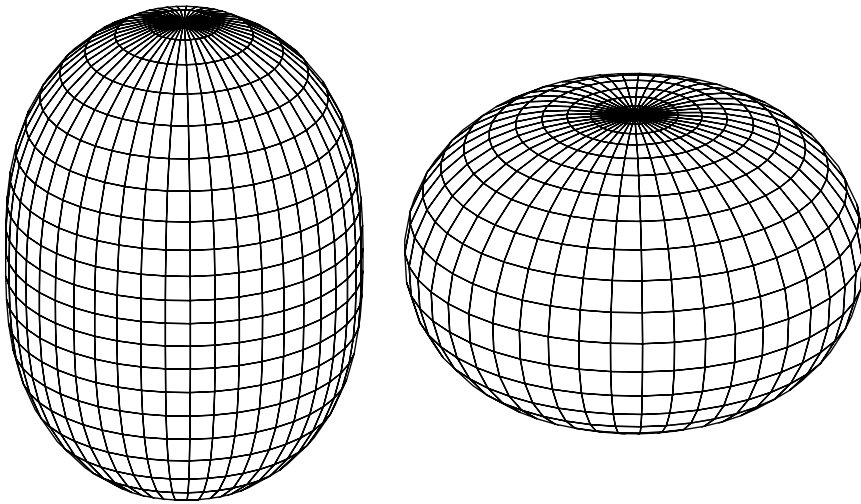


Figure 8.13 A highly exaggerated picture of the normal mode ${}_0S_2$. This mode has a period of about 54 minutes; the two images are separated in time by 27 minutes.

for obvious reasons. The toroidal mode ${}_0T_1$ represents a change in Earth's rotation rate; this can happen but occurs at such long time intervals that it is unimportant in seismology. The toroidal mode ${}_0T_2$ has a period of about 44 minutes and describes a relative twisting motion between the northern and southern hemispheres. Because of the fluid outer core, toroidal modes do not penetrate below the mantle.

Although theoretical solutions for the normal modes of a solid sphere date back to Lamb in 1882, definitive observations for the Earth did not occur until the great 1960 earthquake in Chile. The enormous size of this event (the largest since seismographs began recording about a century ago), together with improvements in instrument design at long periods, made it possible to identify a few dozen normal modes. The next two decades were perhaps the golden age in normal mode seismology as over a thousand modes were identified (e.g., Gilbert and Dziewonski, 1975) and new methods were derived for inverting the observations for Earth structure (e.g., Backus and Gilbert, 1967, 1968, 1970).

The normal mode eigenfrequencies are identical for different azimuthal order number m only for a spherically symmetric solid (this is called *degeneracy* in the eigenfrequencies). Earth's small departures from spherical symmetry (e.g., ellipticity, rotation, general 3-D velocity variations) will cause the eigenfrequencies to separate. This is termed *splitting*; a single spectral peak will split into a *multiplet* composed of the separate peaks for each value of m . Earth's rotation rate and ellipticity are well known, but splitting due to 3-D structure is also observed, so measurements of mode splitting can be using to constrain three-dimensional velocity variations.

As an example of normal mode observations, Figure 8.14 plots the spectrum of 240 hours of data from the 2004 Sumatra-Andaman earthquake recorded on the vertical component of station ARU in Russia. The low-order spheroidal modes (labeled) are seen with excellent signal-to-noise because of the size of this earthquake ($M_W = 9.1$, the largest since the 1964 Alaskan earthquake and the first giant subduction zone earthquake to be recorded by modern broadband seismometers). Many of the modes are clearly split and ${}_0S_2$ is shown at an expanded scale to illustrate its splitting into five peaks, corresponding to its five m values, i.e., ${}_0S_2^{-2}$, ${}_0S_2^{-1}$, etc. The regular spacing of these peaks in the ${}_0S_2$ multiplet is characteristic of splitting due to Earth's rotation. Modes ${}_3S_1$ and ${}_1S_3$ have slightly different center frequencies but overlap so much that they cannot be separately resolved.

Since wave motion in the Earth can be described to equal precision with either traveling waves or normal modes, what is the advantage of the normal mode approach? Largely it comes from analysis of long time series from large events, where the multiplicity of different phase arrivals makes a traveling wave representation awkward. For example, it would be extremely difficult to attempt to model all of the

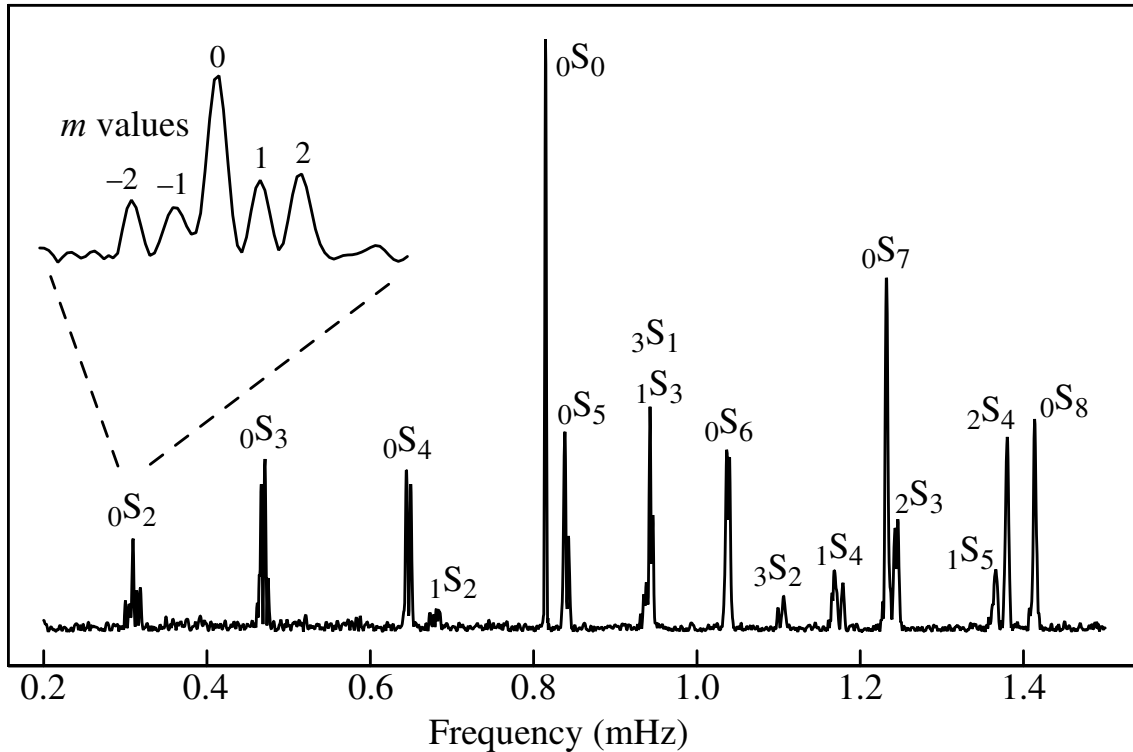


Figure 8.14 Low-order spheroidal modes visible in the spectrum of 240 hours of data from the 2004 Sumatra-Andaman earthquake ($M_W = 9.1$) recorded at station ARU at Arti, Russia (courtesy of Guy Masters). Mode $0S_2$ is plotted at an expanded scale from 0.29 to 0.33 mHz to show its splitting into a five-peaked multiplet, corresponding to azimuthal order number (m) values from -2 to 2.

arrivals visible in Figure 8.9 with a time domain approach. However, by taking the Fourier transform of individual records and measuring the position of the spectral peaks (and any splitting that can be observed), it is possible to identify the various modes and use them to constrain Earth structure. This is the only practical way to examine records at very long periods (> 500 s) and provides information about the Earth's density structure that cannot be obtained any other way. Normal modes also are able to examine Earth properties, such as the shear response of the inner core, that are difficult to observe directly with body waves. Attenuation causes the mode amplitudes to decay with time, and so normal mode observations help to constrain Q at very long periods. Finally, normal modes provide a complete set of basis functions for the computation of synthetic seismograms that naturally account for Earth's sphericity. Computing synthetic seismograms by summing normal modes is standard practice in surface-wave and long-period body-wave seismology. The number of modes required increases rapidly at higher frequencies, but with modern computers, normal mode summation is an increasingly attractive alternative to other methods.